

# Acceleration Mechanics in Relativistic Shocks by the Weibel Instability

K.-I. Nishikawa

*National Space Science and Technology Center, Huntsville, AL 35805*

`ken-ichi.nishikawa@nsstc.nasa.gov`

P. E. Hardee

*Department of Physics and Astronomy, The University of Alabama, Tuscaloosa, AL 35487*

`phardee@bama.ua.edu`

C. B. Hededal

*Dark Cosmology Center, Niels Bohr Institute, Juliane Maries Vej 30,  
2100 Copenhagen Ø, Denmark*

and

G. J. Fishman

*NASA-Marshall Space Flight Center,  
National Space Science and Technology Center, Huntsville, AL 35805*

## ABSTRACT

Plasma instabilities (e.g., Buneman, Weibel and other two-stream instabilities) created in collisionless shocks may be responsible for particle (electron, positron, and ion) acceleration. Using a 3-D relativistic electromagnetic particle (REMP) code, we have investigated long-term particle acceleration associated with relativistic electron-ion or electron-positron jet fronts propagating into an unmagnetized ambient electron-ion or electron-positron plasma. These simulations have been performed with a longer simulation system than our previous simulations in order to investigate the nonlinear stage of the Weibel instability and its particle acceleration mechanism. The current channels generated by the Weibel instability are surrounded by toroidal magnetic fields and radial electric

fields. This radial electric field is quasi stationary and accelerates particles which are then deflected by the magnetic field. Whether particles are accelerated or decelerated along the jet propagation direction depends on the velocity of particles and the sign of  $\mathbf{E} \times \mathbf{B}$  in the moving frame of each particle. For the electron-ion case the large scale current channels generated by the ion Weibel instability lead to more acceleration near the jet head. Consequently, the accelerated jet electrons in the electron-ion jet have a significant hump above a thermal distribution. However, in the electron-positron case, accelerated jet electrons have more smooth nearly thermal distribution. In the electron-positron case, initial acceleration occurs as current channels form and then continues at a much lesser rate as the current channels and corresponding toroidal magnetic fields generated by the Weibel instability dissipate.

*Subject headings:* relativistic jets: Weibel instability - shock formation - electron-ion plasma, particle acceleration - particle-in-cell

## 1. Introduction

Radiation observed from astrophysical systems containing relativistic jets and shocks, e.g., active galactic nuclei (AGNs), gamma-ray bursts (GRBs), and Galactic microquasar systems usually has nonthermal emission spectra. In most of these systems, the emission is usually thought to be generated by accelerated electrons through the synchrotron (jitter) and/or inverse Compton mechanisms. Radiation from these systems is often observed in the radio through the gamma-ray region. Radiation in optical and higher frequencies typically requires continual strong particle acceleration in order to counter radiative losses. It has been proposed that the needed particle acceleration occurs in shocks produced by differences in flow speed within the jet (sometimes referred to as “internal shocks”) (e.g., Piran 2005).

Particle-in-cell (PIC) simulations can shed light on the microphysical mechanism of particle acceleration that occurs in the complicated dynamics within relativistic shocks. Recent PIC simulations of relativistic electron-ion jets show acceleration occurring within the downstream jet, but not likely by the scattering of particles back and forth across the shock, as in Fermi acceleration (Frederiksen et al. 2003, 2004; Nishikawa et al. 2003, 2005; Hededal et al. 2004; Hededal & Nishikawa 2005; Silva et al. 2003; Jaroschek et al. 2005). In general, these independent simulations have confirmed that relativistic jets propagating through a weakly or non magnetized ambient plasma excite the Weibel instability (Weibel 1959). This instability generates current filaments and associated magnetic fields (Medvedev & Loeb 1999; Brainerd 2000; Pruet et al. 2001; Gruzinov 2001), and accelerates electrons

(Silva et al. 2003; Frederiksen et al. 2003, 2004; Nishikawa et al. 2003, 2005; Hededal et al. 2004; Hededal & Nishikawa 2005).

In this paper we present new simulation results of particle acceleration and magnetic field generation in relativistic jet shocks using a 3-D relativistic electromagnetic particle-in-cell (REMP) code. Our new simulations with additional diagnostics allow us to examine the mechanism of particle acceleration in detail, e.g., Hededal et al. (2004).

At the end of our simulations we see four different regions. From the beginning of interaction outwards to the jet front the regions are: (1) a linear instability growth region, (2) a nonlinear saturation region, (3) a nonlinear dissipation region, and (4) the head region of the relativistic jet. The instability generates current filaments elongated along the streaming direction with associated transverse toroidal magnetic fields. The charge separation accompanying the current filaments produces radial electric fields which are mainly perpendicular to the toroidal transverse magnetic fields. Particles are accelerated and decelerated in parallel and perpendicular directions relative to their initial motion by the transient force due to the radial electric field and the Lorentz force from the transverse magnetic field. In §2 the simulation model and initial conditions are described. The simulation results are presented in §3, and in §4 we summarize and discuss the new results.

## 2. Simulation Setup

The code used in this study is a modified version of the TRISTAN code, a relativistic electromagnetic particle (REMP) code (Buneman 1993). Descriptions of PIC codes are presented in Dawson (1983), Birdsall & Langdon (1995), and Hickory & Eastwood (1988). This code has been used previously for many applications including astrophysical plasmas (Zhao et al. 1994; Nishikawa et al. 1997).

Two simulations were performed using a system with  $(N_x, N_y, N_z) = (85, 85, 640)$  cells and a total of  $\sim 380$  million particles (27 particles/cell/species for the ambient plasma) in the active grid zones. In the simulations the electron skin depth,  $\lambda_{ce} = c/\omega_{pe} = 9.6\Delta$ , where  $\omega_{pe} = (4\pi e^2 n_e / m_e)^{1/2}$  is the electron plasma frequency and  $\Delta$  is the grid size. Here the computational domain is two times longer than in our previous simulations (Nishikawa et al. 2003, 2005). In both simulations the electron number density of the jet is  $0.741n_e$ , where  $n_e$  is the ambient electron density and as in the previous work  $\gamma = 5$  (Nishikawa et al. 2003, 2005). In both simulations jets are injected in a plane across the computational grid at  $z = 25\Delta$  in the positive  $z$  direction in order to any eliminate effects associated with the boundary conditions at  $z = z_{\min}$ . Radiating boundary conditions were used on the planes at  $z = z_{\min}$  &  $z_{\max}$ . Periodic boundary conditions were used on all transverse

boundaries (Buneman 1993). The ambient and jet electron-positron plasma has mass ratio  $m_{e^-}/m_{e^+} = 1$ , and the electron-ion plasma ( $e^-/i^+$ ) has mass ratio  $m_i/m_e = 20$ . The electron/positron thermal velocity in the ambient plasma is  $v_{th}^e = 0.1c$  and the ion thermal velocity is  $v_{th}^i = 0.022c$  where  $c$  is the speed of light.

As in previous papers (Nishikawa et al. 2003, 2005) the “flat” (thick) jet fills the computational domain in the transverse directions (infinite width). Thus, we are simulating a small section of a relativistic shock infinite in the transverse direction. The present choice of parameters and simulations allows comparison with previous simulations (Silva et al. 2003; Frederiksen et al. 2003, 2004; Nishikawa et al. 2003, 2005; Hededal et al. 2004; Hededal & Nishikawa 2005). If the simulations are scaled to the interstellar medium (ISM), the electron skin depth becomes  $c/\omega_{pe} \sim 3 \times 10^8 \text{ m s}^{-1}/50,000 \text{ Hz} \sim 6,000 \text{ m}$  and the length of the simulation box is about  $4 \times 10^5 \text{ m}$  ( $= 400 \text{ km}$ ).

### 3. Simulation results

The jet makes contact with the ambient plasma at a 2D interface spanning the computational domain. Here the dynamics of the propagating jet head and the formation of a shock region is studied. Effectively we study the evolution of the Weibel instability of a small portion of a much larger shock in a spatial and temporal way that includes the motion of the jet head and the spatial development of nonlinear saturation and dissipation from the injection point to the jet front defined by the fastest moving jet particles.

Figure 1 shows components of the current density resulting from development of the Weibel instability behind the jet front at time  $t = 19.5/\omega_{pe}$  [panels (a)  $e^-/i^+$  & (c)  $e^-/e^+$ ] and at time  $t = 59.8/\omega_{pe}$  [panels (b)  $e^-/i^+$  & (d)  $e^-/e^+$ ]. The arrows show the  $z$  and  $x$  components of the current density and the color scale also shows the  $z$  component of the current density. The intensities and arrow lengths are scaled so that small values can be seen in each panel and cannot be directly intercompared. Panels 1a ( $e^-/i^+$ ) and 1c ( $e^-/e^+$ ) where the  $z$  component dominates indicate the initial linear growth of the Weibel instability. The current channels generated by the Weibel instability in the electron-positron case show considerable dissipation at the later time at large distance (panel 1d). This result is indicated by the lower values of  $j_z$  and disorganized orientation of the arrows,  $j_{x,z}$  current components, for  $z/\Delta > 270$ . On the other hand, the current channel(s) in the electron-ion case remain well organized at the larger distances at this later time (panel 1b).

Figure 2 indicates magnetic field structure and field energy along the  $z$  direction at time  $t = 59.8/\omega_{pe}$ . Panels 2a ( $e^-/i^+$ ) and 2c ( $e^-/e^+$ ) show 1-D cuts through the computational grid parallel to the  $z$ -axis at  $x/\Delta = 43$  and  $y/\Delta = 33, 43$ , and  $53$ . The spacing in  $y$  is about

the electron skin depth ( $\lambda_{ce} \sim 9.6\Delta$ ). This figure provides some quantitative longitudinal information about the filament structures shown qualitatively in Figure 1. With separation by about the electron skin depth, the phase of the instability is different along different 1-D cuts, but the amplitudes are similar. Panel 2c ( $e^-/e^+$ ) shows that  $B_x$  declines for  $z/\Delta > 270$  and dissipates around  $z/\Delta = 480$  in the electron-positron case. This decline coincides with the disorganization in current structure revealed in Figure 1d.  $B_x$  does not similarly decline in the electron-ion case (panel 2a).

In order to examine global changes, the magnetic field energies averaged across the  $x - y$  plane are plotted along the  $z$  direction in panels 2b ( $e^-/i^+$ ) and 2d ( $e^-/e^+$ ). We note that very little magnetic energy is in the parallel magnetic field component. Nonlinear saturation occurs at  $z/\Delta = 340$  in the electron-ion case (panel 2b) and at  $z/\Delta = 270$  in the electron-positron case (panel 2d) (see also Kato 2005). The saturation level in the electron-ion case is about two times higher than in the electron-positron case. While the magnetic field energy is dissipated around  $z/\Delta = 450$  in the electron-positron case, a much smaller reduction is seen in the electron-ion case. Here the ion Weibel instability is excited in the electron-ion case (Hededal et al. 2004) and maintains a large total magnetic field energy which is more than four times of that in the electron-positron case. In the electron-positron case the magnetic fields appear turbulent in the region ( $400 < z/\Delta < 500$ ) as suggested by the current structure seen in Figure 1d.

The acceleration of electrons by the Weibel instability has been reported in previous work (Silva et al. 2003; Frederiksen et al. 2003, 2004; Nishikawa et al. 2003, 2005; Hededal et al. 2004; Hededal & Nishikawa 2005). Some explanation of the acceleration mechanism associated with the development of current channels can be found in Hededal et al. (2004) and Medvedev et al. (2005). Here Figure 3 shows current channel structure in 2D images in the  $x - y$  plane at  $z/\Delta = 430$  and  $t = 59.8/\omega_{pe}$ , which correspond to the nonlinear dissipation region. Panels 3a ( $e^-/i^+$ ) and 3b ( $e^-/e^+$ ) show the  $z$  component of the current density generated by the Weibel instability in color with the  $x$  and  $y$  components of the electric field represented by arrows. Panels 3c ( $e^-/i^+$ ) and 3d ( $e^-/e^+$ ) show the  $z$  component of  $\mathbf{E} \times \mathbf{B}$  along with the  $x$  and  $y$  components of the magnetic field shown as arrows. Panels 3a, 3c, and 3e show that the center of the single ion current channel is located at  $(x/\Delta, y/\Delta) = (35, 72)$ . This ion current channel is surrounded by transverse toroidal magnetic fields indicated by the arrows in panel 3c. This large scale (nearly the ion skin depth ( $43\Delta$ )) current channel is generated by the ion Weibel instability. Further investigation of the nonlinear evolution of the ion Weibel instability requires a larger system such as  $(N_x, N_y, N_z) = (200, 200, 800)$ , (e.g., Frederiksen et al. 2004), that can contain several current channels in the transverse direction and be sufficiently long to illustrate the spatial development.

In addition to toroidal magnetic fields, radial electric fields accompany the charge separation associated with the current channels (Milosavljević, Naker, & Spitkovsky 2005). These electric fields are indicated by the arrows in panels 3a ( $e^-/i^+$ ) and 3b ( $e^-/e^+$ ). The electric and magnetic fields are approximately perpendicular in the  $x-y$  plane. The  $z$  component of  $\mathbf{E} \times \mathbf{B}$  in the simulation/ambient rest frame is mainly positive (see panels 3c and 3d) on the  $x-y$  plane at this time and indicates the direction of motion of particles accelerated by the radial electric fields as modified by the Lorentz force due to the transverse magnetic fields. It should be noted that the transient acceleration due to the radial electric field occurs within one gyromotion. Therefore, the resultant motion is not identical to the  $\mathbf{E} \times \mathbf{B}$  drift which takes place over many gyromotions. Still the sign of the  $z$  component of  $\mathbf{E} \times \mathbf{B}$  gives an indication of the average effect of the radial and transverse magnetic fields on the ambient and jet particles. Panels 3c and 3d which show that  $(\mathbf{E} \times \mathbf{B})_z$  is typically in the  $+z$  direction in the ambient reference frame imply that ambient particles accelerated by the radial electric fields are directed by Lorentz forces to move in the  $+z$  direction. Thus, on average ambient particles are accelerated in the  $+z$  direction.

The sign of  $(\mathbf{E} \times \mathbf{B})_z$  depends on the frame of reference through the Lorentz transformation, e.g., Jackson (1999). We have computed the value of  $(\mathbf{E} \times \mathbf{B})_z$  in reference frames moving with  $\beta_z = v_z/c = 0.6, 0.8$  &  $0.9798$  where the third value corresponds to the initial jet particle velocity. The results for  $(\mathbf{E} \times \mathbf{B})_z$  with  $\beta_z = 0.8$  relative to the simulation frame are shown in Panels 3e and 3f. In panels 3e and 3f the arrows indicate the  $x$  and  $y$  components of the magnetic field in the moving reference frame. In these reference frames  $(\mathbf{E} \times \mathbf{B})_z$  is mainly negative. The implication is that particles moving with these higher speeds, when accelerated by the radial electric fields, are on average directed by Lorentz forces to move in the  $-z$  direction in this moving reference frame. In the ambient reference frame this appears as a deceleration. In reality, both spatial and temporal variation in filament structure produces more than a simple average acceleration or deceleration along the flow, and more than simple scattering into the transverse direction. The complicated nature of the particle motion and the acceleration process accompanying the filament structure is illustrated and discussed in Hededal et al. (2004).

Figure 4 shows the phase space distribution of jet and ambient electrons in order to establish how particle acceleration is related to magnetic and electric field spatial development associated with the Weibel instability. The value of  $(\mathbf{E} \times \mathbf{B})_z$  in a frame moving with  $v_z/c \sim 0.8$  becomes more strongly negative in the electron-ion case (Fig. 3e) than in electron-positron case (Fig. 3f). Consequently, a larger average deceleration of jet electrons occurs in the electron-ion case than in electron-positron case shown in Panels 4a and 4b. In the electron-ion case, jet electrons are accelerated in the parallel direction at  $z/\Delta = 495$  not too far behind the jet head (panel 4a). The largest perpendicular acceleration occurs at

$z/\Delta = 330$  where the magnetic field energy achieves a local maximum (see Fig. 2b). Behavior is qualitatively similar to the electron-positron case but maximum values are somewhat reduced. Additionally, the electron-positron case clearly saturates by this simulation time. Panel 4d clearly shows a linear acceleration region ( $130 < z/\Delta \leq 270$ ), a nonlinear region ( $270 < z/\Delta \leq 540$ ), and a jet head region ( $540 < z/\Delta \leq 580$ ). The nonlinear region is contained between the two magnetic field energy peaks at  $z/\Delta = 270$  &  $540$  shown in Figure 2d. By comparison development in the electron-ion case is affected by the transverse dimensions of the grid, i.e., one current channel fills the grid transversely beyond the magnetic energy maximum at  $z/\Delta = 330$ . With this restriction removed, it seems likely that even larger differences would appear between the electron-ion case and electron-positron case (Heddal et al. 2004).

The parallel acceleration of ambient electrons is shown in panels 4e ( $e^-/i^+$ ) and 4f ( $e^-/e^+$ ). At the time  $t = 59.8/\omega_{pe}$  the ambient electrons in the electron-ion case are not accelerated nearly as much as those in the electron-positron case. It seems likely that ambient ion inertia restricts ambient electron parallel acceleration, and the ion Weibel instability is not fully excited (e.g., Heddal et al. 2004). This lack of parallel acceleration can also be a result of insufficient transverse grid dimension. By comparison, in the electron-positron case positrons have the same mass as electrons and the ambient electrons and positrons are fully involved in the Weibel instability with our present grid dimensions.

We need to examine the particle momentum distributions in order to determine whether the instability results in a thermal or a power law distribution. Additionally, it is necessary to examine the particle momentum distributions in the parallel and transverse directions as particle acceleration need not lead to an isotropic distribution. Figure 5 shows momentum distributions of jet electrons at time  $t = 59.8/\omega_{pe}$ . Parallel momentum,  $\gamma_v v_{\parallel}$ , distributions are shown in panels (a)  $e^-/i^+$  and (b)  $e^-/e^+$  and perpendicular momentum distributions,  $\gamma_v v_{\perp}$  are shown in panels (c)  $e^-/i^+$  and (d)  $e^-/e^+$ . In the panels the blue curves show the distribution of jet electrons found by plotting one third of the jet electrons in a portion of the grid near to the inlet ( $25 \leq z/\Delta \lesssim 213$ ) and provides a reasonable indication of the initial injected electron distribution. The red curves show the momentum distribution of jet electrons found by plotting one third of the jet electrons from a region behind the jet front ( $400 \lesssim z/\Delta \lesssim 590$ ) and indicates the accelerated electron distribution. All distributions are plotted in the ambient/simulation rest frame.

The distribution of a Lorentz-boosted thermal electron population is also plotted in Figure 5 as dashed green curves. Here we use a bi-Maxwellian distribution function of the form (see Qin et al. 2005)

$$f(\gamma_v v_{\parallel}, \gamma_v v_{\perp}) = N_{\max} \exp[-(\gamma_v m_e v_{\parallel} - \gamma_u m_e u)^2 / (2\gamma_u^3 m_e k T_{\parallel})] \exp[-(\gamma_v m_e v_{\perp})^2 / (2\gamma_u m_e k T_{\perp})] ,$$

where  $v_{\perp}^2 = v_x^2 + v_y^2$ ,  $\gamma_v = (1 - (v_{\perp}^2 + v_{\parallel}^2)/c^2)^{-1/2}$  is the Lorentz factor for electrons, and  $\gamma_u = (1 - (u/c)^2)^{-1/2}$  is the bulk (averaged) Lorentz factor. This particular form presupposes that the electrons are “cold”, i.e.,  $m_e c^2/(kT) > 1$ , in the jet rest frame. The parallel and perpendicular thermal distributions that provide a best fit to the observed parallel and perpendicular distributions are calculated separately but use the same bulk Lorentz factor,  $\gamma_u$ . The bulk Lorentz factor, different for the electron-ion and electron-positron cases, is found by fitting the parallel momentum distributions (red curves in panels (5a) and (5b)). Note that the perpendicular velocity of jet electrons appears as a secondary effect through  $\gamma_v$  in the parallel momentum distributions. Our best fits require a bulk Lorentz boost of  $\gamma_u u \sim 3.0$  and  $3.8$  for  $e^-/i^+$  and  $e^-/e^+$  cases, respectively, i.e., more electron slowing for the electron-ion case. The accompanying parallel temperatures are  $T_{\parallel} = 1.16 \times 10^9$  K and  $0.72 \times 10^9$  K for  $e^-/i^+$  and  $e^-/e^+$  cases, respectively, i.e., hotter for the electron-ion case. The accompanying perpendicular temperatures are  $T_{\perp} = 9.59 \times 10^9$  K and  $4.79 \times 10^9$  K for  $e^-/i^+$  and  $e^-/e^+$  cases, respectively, i.e., again hotter for the electron-ion case. In both  $e^-/i^+$  and  $e^-/e^+$  cases  $T_{\perp} > T_{\parallel}$ . Note that these fitted temperatures imply a “warm” jet electron plasma, i.e.,  $kT \sim m_e c^2$ , and formally the assumption that the temperatures are cold is violated. Nevertheless, the comparisons remain qualitatively if not quantitatively robust.

The electron-ion case shows a significant hump at  $\gamma v_{\parallel} = 10$ , which is found in the parallel velocity distribution for the electron-ion case (panel 5a). The electron-positron case (panel 5b) shows a smoother higher energy tail without a noticeable hump. The hump could be due to more effective acceleration near the jet head (near  $z\Delta = 490$ ) as shown in Fig. 4a, also indicated by Fig. 2 in Hededal et al. (2004). This more effective acceleration in the electron-ion case is also indicated by the higher fitted perpendicular temperature in the electron-ion case (see panels 5c and 5d).

The differences in parallel and perpendicular momentum distributions between electron-ion and electron-positron cases provides a potential discriminator between electron-ion and electron-positron shocks. In particular, differences in the momentum distributions will appear as differences in the radiation spectrum (Hededal 2005, Hededal & Nordlund 2005). Such potential spectral differences will be in addition to more subtle differences induced by differences in magnetic field strength and structure.

#### 4. Summary and Discussion

We have performed self-consistent, three-dimensional relativistic particle simulations of relativistic electron-positron and electron-ion jets propagating into unmagnetized electron-positron and electron-ion ambient plasmas, respectively. The present simulations were per-



formed using a larger simulation system and for a longer time compared to our previous simulations (Nishikawa et al. 2003, 2005). The larger grid and longer time allowed us to investigate the nonlinear development of the Weibel instability and the accompanying acceleration mechanism. The Weibel instability forms current filaments and accompanying transverse toroidal magnetic fields around the current filaments. Electrons deflected by the perturbed (small) transverse magnetic fields accompanying the current filaments subsequently enhance the current filaments (Weibel 1959; Medvedev & Loeb 1999; Brainerd 2000; Gruzinov 2001). The acceleration of particles by electric fields toward or away from the current filaments and deflection of particles due to the Lorentz force increases as the magnetic field perturbation grows in amplitude. Basically we see that the transient force due to the radial electric field with circular magnetic field leads to acceleration in the perpendicular direction relative to the initial motion, and an average deceleration in the parallel direction but with an acceleration of some electrons in the parallel direction to produce a high energy thermal distribution. It should be noted that the Weibel instability is convective, i.e., the real part of the frequency is zero and current filaments grow temporally in the appropriate rest frame (Medvedev & Loeb 1999; Nishikawa et al. 2003, 2005). In our simulations the values of  $(\mathbf{E} \times \mathbf{B})$  fluctuate highly in a spatial sense in both ambient and jet reference frames. Our results here are consistent with results from previous simulations (Frederiksen et al. 2003, 2004; Hededal et al. 2004; Nishikawa et al. 2003, 2005; Hededal & Nishikawa 2005).

The present simulations show no clear sign of Fermi acceleration and the main acceleration of electrons takes place in the transition region behind the jet head. Processes in the relativistic collisionless shock are dominated by current structures produced by the Weibel instability. This instability is first excited near to the jet injection plane and grows spatially from smaller to larger current filaments behind the propagating jet front. Radial electric fields accompany the development of current channels and toroidal transverse magnetic fields around the current channels. The toroidal magnetic and radial electric fields associated with the current filaments accelerate and decelerate jet electrons and positrons. In the electron-positron case the organized current channels and accompanying fields reach a maximum and then dissipate and become more disordered. Particle acceleration/deceleration effects decrease in the dissipation region behind the jet front. Here we note that other new simulations (see Nishikawa et al. 2005a) show that the level of magnetic field in the dissipation region depends on the initial jet Lorentz factor or the Lorentz factor distribution. On average bulk jet electron motion is decelerated in the parallel direction while some jet particles are accelerated in the parallel direction to form a nearly thermal distribution ( $e^-/e^+$ ) or a thermal distribution with a hump in higher energy ( $e^-/i^+$ ). Deceleration in the parallel direction is accompanied by large acceleration in the perpendicular directions. The ambient

electron-positron medium is on average accelerated in the jet direction in the interaction. In the electron-ion case the instability evolves spatially similar to the electron-positron case but here large scale ion current channels are ultimately generated by the ion Weibel instability in the electron-ion jet (see also Frederiksen et al. 2004; Hededal et al. 2004). In this case more bulk deceleration, a prominent humped high energy tail in the parallel direction, and more transverse acceleration occur for the jet electrons. Very little acceleration of the ambient electrons in the electron-ion jet is observed on the simulation grid. It is clear that a larger simulation grid is necessary to follow non-linear development in the electron-ion case for a longer time.

The efficiencies of conversion of bulk kinetic energy into radiation via synchrotron or “jitter” emission from relativistic shocks is determined by the magnetic field strength and structure, and by the electron energy distribution behind the shock (Medvedev 2000; Hededal 2005). Whether the radiation is in the synchrotron or jitter regime depends only on the nature of the magnetic field. If the typical fluctuation spatial scale of the magnetic field is smaller than the expected gyro-orbit, and the magnetic field is turbulent (power law distributed) then the radiation is in the jitter regime (Hededal 2005; Hededal & Nordlund 2005). The radiation spectrum from the accelerated electrons in the Weibel generated electromagnetic field shows good agreement with observations (Piran 2005; Hededal 2005, Hededal & Nordlund 2005).

The fundamental microscopic characteristics of relativistic shocks are essential for a proper understanding of the prompt gamma-ray and afterglow emission in gamma-ray bursts, and also to an understanding of the particle reacceleration processes and emission from the shocked regions in relativistic AGN jets. Obviously the accelerated particle distribution both parallel and perpendicular to the bulk motion needs to be known and, in particular the generation of magnetic field and its structure in the shock needs to be known. Since the shock dynamics is complex and subtle at the microscopic level, more comprehensive studies are required to better understand the acceleration of electrons, the generation of magnetic fields, magnetic field structure and the associated emission. This further study will provide the insight into basic relativistic collisionless shock characteristics needed to provide a firm physical basis for modeling the emission from shocks in relativistic flows.

K.I. Nishikawa was a NRC Senior Research Fellow at NASA Marshall Space Flight Center until June 2005. K.I. Nishikawa’s research is partially supported by the National Science Foundation through awards ATM 9730230, ATM-9870072, ATM-0100997, INT-9981508, and AST-0506719 to the University of Alabama in Huntsville. P. Hardee acknowledges National Science Foundation support through award AST-0506666 and the National Space Science & Technology Center (NSSTC/MSFC) through award NCC8-256 to The University of Al-

abama. The simulations have been performed on IBM p690 (Copper) at the National Center for Supercomputing Applications (NCSA) which is supported by the National Science Foundation.

## REFERENCES

- Birdsall, C.K., & Langdon, A.B., 1995, Plasma Physics via Computer Simulation, McGraw-Hill, second Edition
- Brainerd, J.J. 2000, ApJ, 538, 628
- Buneman, O., 1993, Tristan, in Computer Space Plasma Physics: Simulation Techniques and Software, edited by H. Matsumoto & Y. Omura, p. 67, Terra Scientific Publishing Company, Tokyo
- Dawson, J.M. 1983, Rev. Mod. Phys., 55, 403
- Frederiksen, J.T., Hededal, C.B., Haugbølle, T., & Nordlund, Å. 2003, Proc. From 1st NBSI on Beams and Jets in Gamma Ray Bursts, held at NBIfAFG/NORDITA, Copenhagen, Denmark, August, 2002, (astro-ph/0303360)
- Frederiksen, J.T., Hededal, C.B., Haugbølle, & Nordlund, Å. 2004, ApJ, 608, L13
- Gruzinov, A. 2001, ApJ, 563, L15
- Hickory, R.W., & Eastwood, J.W., 1988, Computer Simulation using Particles, McGraw-Hill, second edition
- Hededal, C.B., 2005, PhD thesis (astro-ph/0506559)
- Hededal, C.B., & Nishikawa, K.-I., 2005, ApJ, 623, L89
- Hededal, C.B., & Nordlund, Å. 2005, submitted to ApJL (astro-ph/0511662)
- Hededal, C.B., Haugbølle, Frederiksen, J.T., & Nordlund, Å. 2004, ApJ, 617, L107
- Jaroschek, C. H., Lesch, H., & Treumann, R. A. 2005, ApJ, 618, 822
- Kato, T. N. 2005, Phys. Plasmas, 12, 080705
- Medvedev, M.V., Fiore, M., Fonseca, R. A., Silva, L. O., & Mori, W.B., 2005, ApJ, 618, L75
- Medvedev, M.V. 2000, ApJ, 540, 704

- Medvedev, M.V. & Loeb, A. 1999, ApJ, 526, 697
- Milosavljević, M., Nakar, E., & Spitkovsky, A. 2005, (astro-ph/0507553)
- Nishikawa, K.-I., Zhao, J., Sakai, J.I., & Neubert, T. 1997a, Adv. Space. Res., 19, (1)117
- Nishikawa, K.-I., Hardee, P., Richardson, G., Preece, R., Sol, H., & Fishman, G.J. 2003, ApJ, 595, 555
- Nishikawa, K.-I., Hardee, P., Hededal, C. B., Richardson, G., Preece, R., Sol, H., & Fishman, G.J. 2005, ApJ, 622, 927
- Nishikawa, K.-I., Ramirez-Ruiz, E., Hardee, P., Hededal, C. B., Fishman, G.J., & Kouveliotou, C. 2005a, ApJ, in preparation
- Piran, T., 2005, To appear in the proceedings of Magnetic Fields in the Universe, Angra dos Reis, Brazil, Nov. 29-Dec 3, 2004, Ed. E. de Gouveia del Pino (astro-ph/0503060)
- Pruet, J., Abazajian, K., Fuller, G. M. 2001, Phys. Rev. D., 64, 063002-1
- Qin, H., Davidson, R.C., Startsev, E., & Lee, W. Wei-li 2005, Princeton Plasma Physics Laboratory preprint (nonneutral.pppl.gov/pdfpapers/PAC2001.FOAB008.pdf)
- Silva, L. O., Fonseca, R. A., Tonge, J.W., Dawson, J. M., Mori, W.B., & Medvedev, M. V., 2003, ApJ, 596, L121
- Weibel, E.S. 1959, Phys. Rev. Lett., 2, 83
- Zhao, J., Sakai, J.I., Nishikawa, K.-I., & Neubert, T. 1994, Phys. Plasmas, 1, 4114

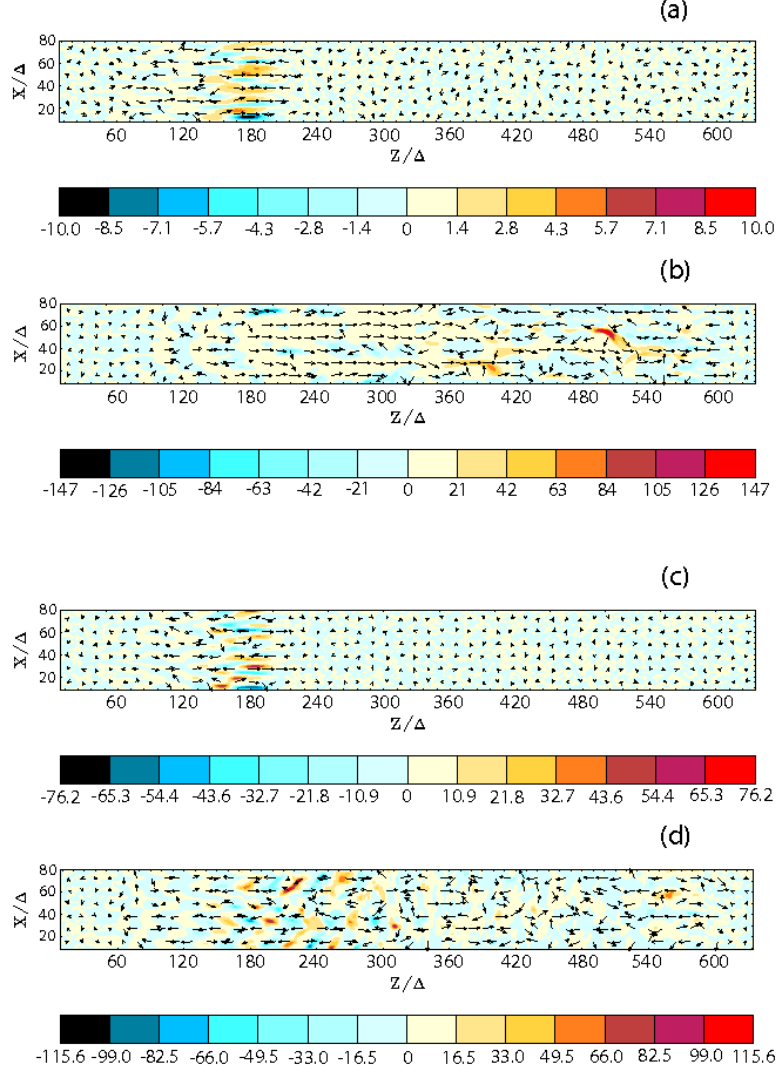


Fig. 1.— 2D images in the  $x - z$  plane at  $y = 43\Delta$  for the electron-ion (panels a & b) and electron-positron (panels c & d) jets injected into an unmagnetized ambient plasma at  $t = 19.5/\omega_{pe}$  (panels a & c), and  $59.8/\omega_{pe}$  (panels b & d). The colors indicate the  $z$  component of current density generated by the Weibel instability with the  $z$  and  $x$  components of current density represented by arrows.

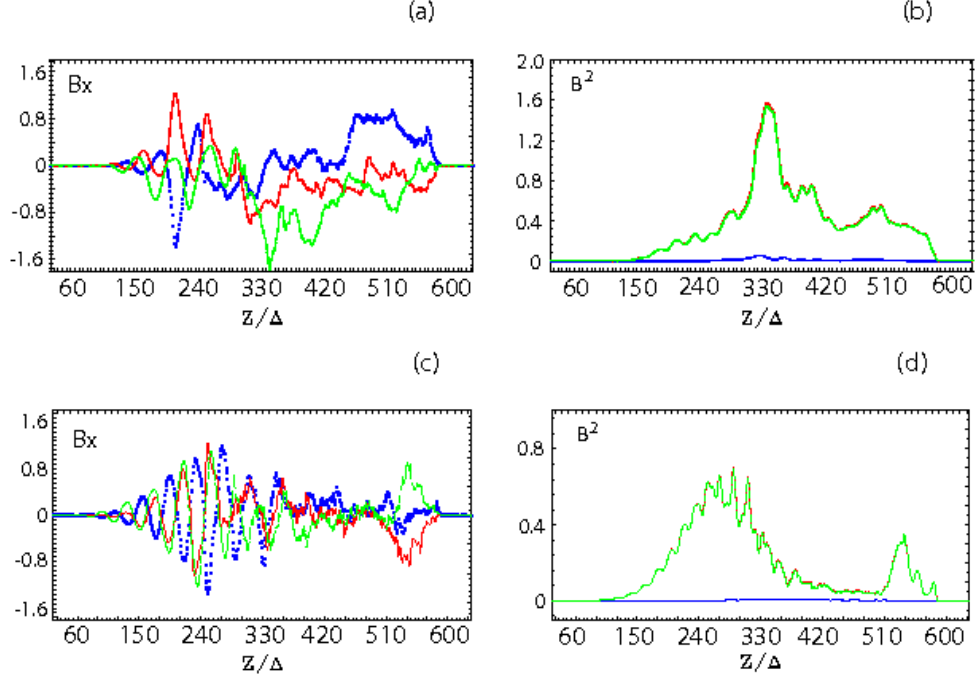


Fig. 2.— 1-D cuts along the  $z$ -direction of the  $x$ -component of the magnetic field (panels a & c), and magnetic field energies (panels b & d) at  $t = 59.8/\omega_{pe}$  for the electron-ion (panels a & b) and electron-positron (panels c & d) jets. 1D cuts for (panels a & c) are at  $x/\Delta = 38$  and  $y/\Delta = 33$  (*blue*), 43 (*red*), 53 (*green*), and cuts are separated by about an electron skin depth. In panels b & d the green curves show the perpendicular magnetic field energy ( $B_{\perp} = B_x^2 + B_y^2$ ). Since the parallel magnetic field energy (blue) is small, the curves of the total magnetic field energy (red) underlie the perpendicular energy curves (green). The units are simulation units.

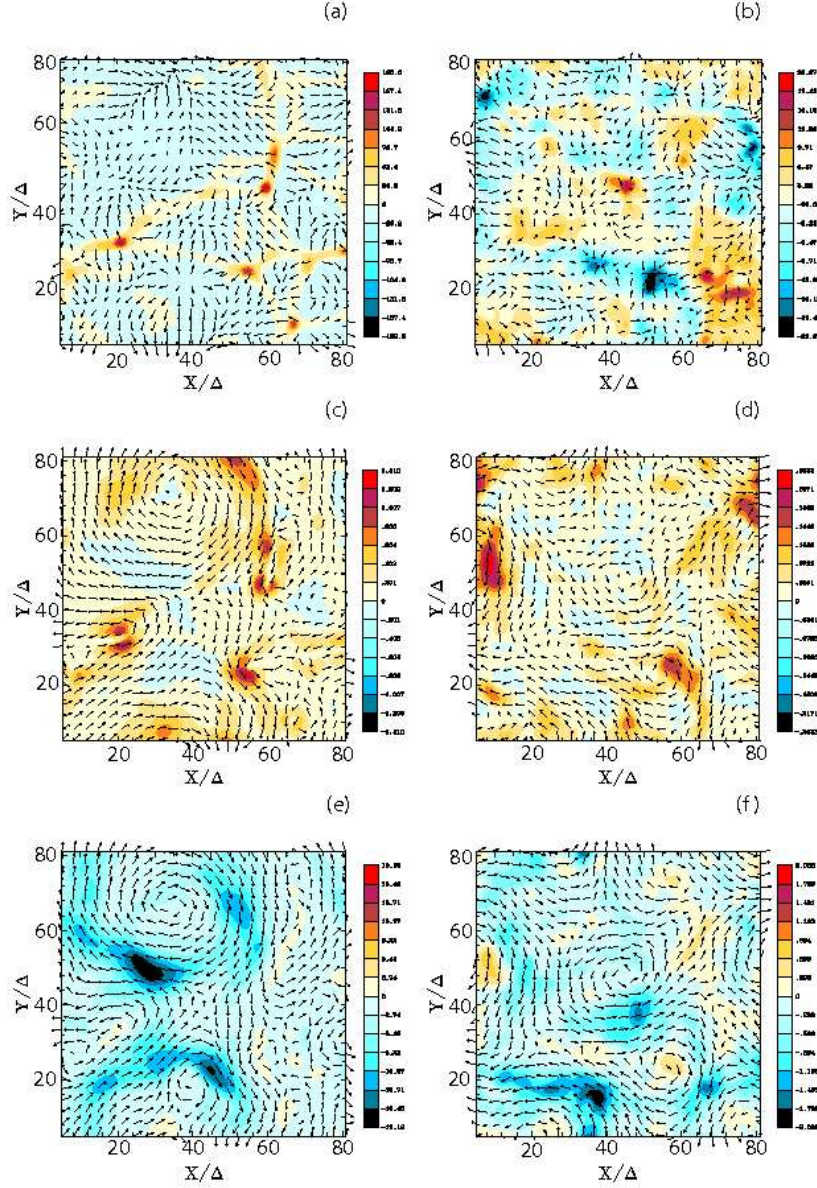


Fig. 3.— 2D images in the  $x - y$  plane at  $Z/\Delta = 430$  for the electron-ion case (left column) and electron-positron case (right column) at  $t = 59.8/\omega_{pe}$ . In panels a & b the colors indicate the  $z$  component of current density with the  $x$  and  $y$  components of the electric field represented by arrows. The middle panels (c & d) show the  $z$  component of  $\mathbf{E} \times \mathbf{B}$  with the  $x$  and  $y$  components of magnetic field indicated by the arrows in the grid rest frame. The bottom panels (e & f) show the  $z$  component of  $\mathbf{E} \times \mathbf{B}$  and  $B_{x,y}$  (by the arrows) in the jet rest frame moving with  $\beta_z = v_z/c = 0.8$ .

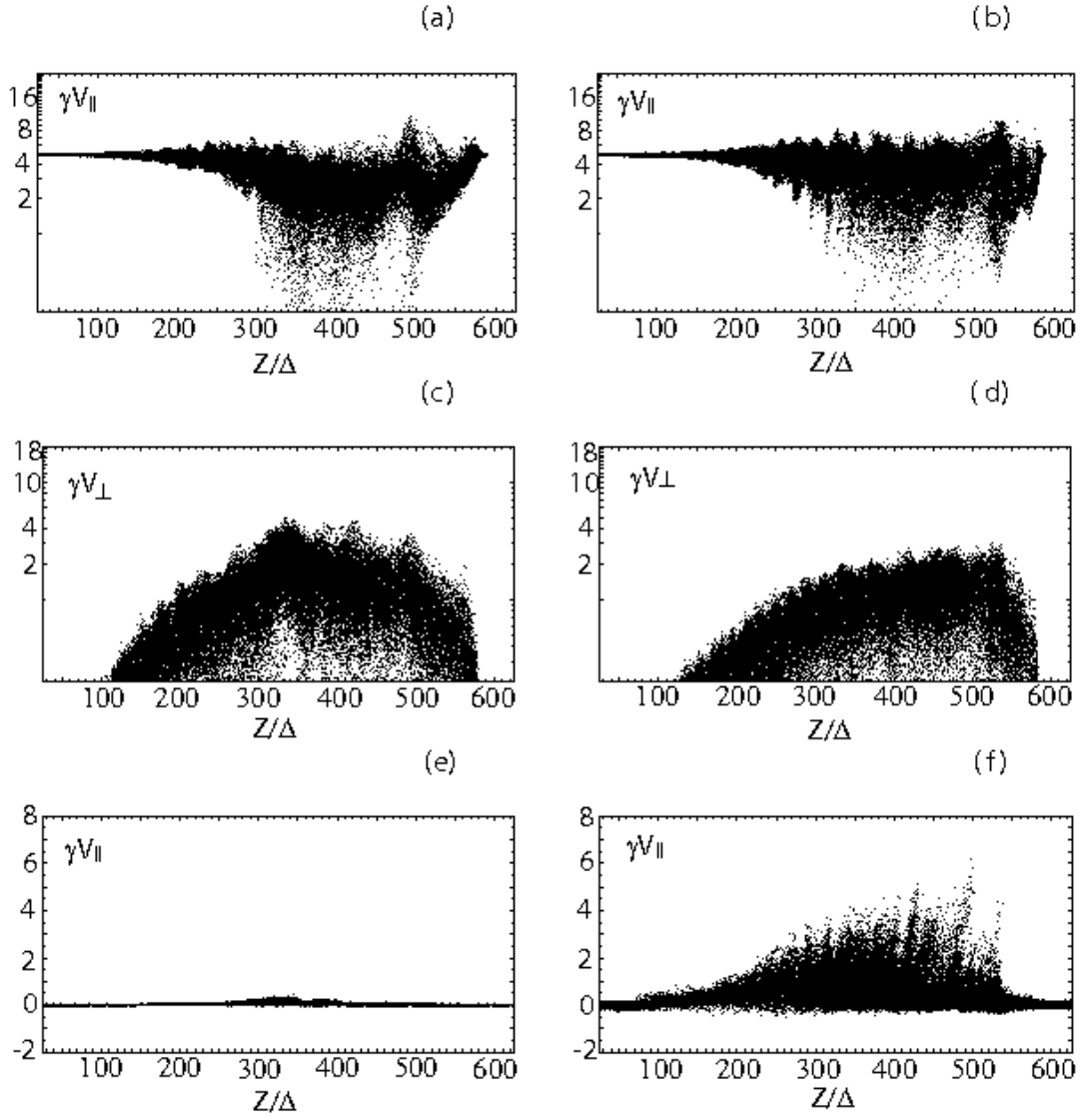


Fig. 4.— Phase space distributions as a function of  $z$  are plotted for the electron-ion (left column) and electron-positron (right column) cases. Jet electrons in  $Z/\Delta - \gamma V_{\parallel}$  and  $Z/\Delta - \gamma v_{\perp}$  phase space at  $t = 59.8/\omega_{pe}$  are plotted in top row and middle row, respectively. In the bottom row the ambient electrons in  $Z/\Delta - \gamma V_{\parallel}$  phase space are plotted.



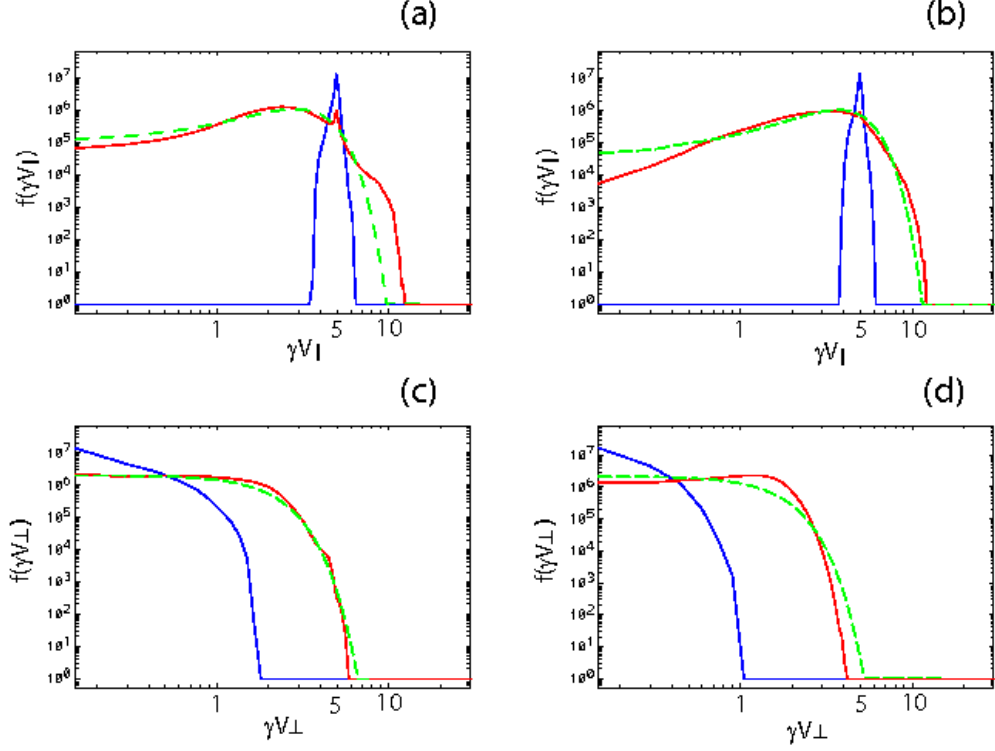


Fig. 5.— Jet electron parallel (panels a & b) and perpendicular (c & d) momentum distributions are plotted at  $t = 59.8/\omega_{pe}$ . The accelerated jet electron distribution is shown by red curves and the initial distribution by blue curves for the electron-ion (panels a & c) and electron-positron (panels b & d) cases. The dashed green curves show a best fit Lorentz-boosted thermal electron distribution in the parallel and perpendicular directions. The zero count on the logarithmic scale is set to 1.